Charged-particle acceleration and energy loss in laser-produced plasmas

D. G. Hicks,[a] C. K. Li, F. H. Séguin, A. K. Ram, J. A. Frenje, and R. D. Petrasso[b]
Plasma Science and Fusion Center, Massachusetts Institute of Technology, Massachusetts 02139

J. M. Soures, V. Yu. Glebov, D. D. Meyerhofer, S. Roberts,
C. Sorce, and C. Stöckl
Laboratory for Laser Energetics, University of Rochester, Rochester, New York 14623

T. C. Sangster and T. W. Phillips
Lawrence Livermore National Laboratory, Livermore, California 94550

(Received 27 April 2000; accepted 22 June 2000)

Spectral measurements have been made of charged fusion products produced in deuterium + helium-3 filled targets irradiated by the OMEGA laser system [T. R. Boehly *et al.*, Opt. Commun. **133**, 495 (1997)]. Comparing the energy shifts of four particle types has allowed two distinct physical processes to be probed: Electrostatic acceleration in the low-density corona and energy loss in the high-density target. When the fusion burn occurred during the laser pulse, particle energy shifts were dominated by acceleration effects. Using a simple model for the accelerating field region, the time history of the target electrostatic potential was found and shown to decay to zero soon after laser irradiation was complete. When the fusion burn occurred after the pulse, particle energy shifts were dominated by energy losses in the target, allowing fundamental charged-particle stopping-power predictions to be tested. The results provide the first experimental verification of the general form of stopping power theories over a wide velocity range. © *2000 American Institute of Physics.* [S1070-664X(00)03012-3]

I. INTRODUCTION

The direct-drive approach to inertial-confinement fusion (ICF) involves the laser-driven implosion of spherical targets to achieve large increases in temperature and density. Under these conditions, copious thermonuclear fusion reactions can occur: the University of Rochester's OMEGA laser system[1] has attained neutron yields of $\sim 10^{14}$ in deuterium-tritium (DT) targets and $\sim 10^{12}$ in deuterium (D_2) targets.[2] Such high yields allow high-resolution spectroscopy of the charged fusion products. These particles, produced inside the fuel region, must pass through the fuel and shell plasma, as well as the corona where strong electric fields may exist. As a result, the energy spectrum of charged fusion products can reflect the physics of slowing down in high-density plasmas, as well as the behavior of electrostatic fields in the target corona. Since the number density of fusion products passing through the target and corona is generally much smaller than typical plasma number densities, fusion products can be treated as test particles which do not perturb the surrounding plasma conditions. This greatly simplifies the interpretation of their spectra.

Strong electric fields are created when hot electrons, generated by laser-plasma instabilities in the corona, escape into the surrounding vacuum. Maintaining quasi-neutrality, electric fields are setup which accelerate plasma ions to suprathermal velocities.[3,4] Extensive literature exists on measurements of such fast ions.[5,6] The related acceleration of fusion products (DT alphas and DD protons) from ICF targets was observed previously[7,8] in studies that used laser wavelengths of 1.05 μm and intensities $>5\times10^{15}$ W/cm^2. By measuring the energy shifts of DT alphas produced at different times and using extensive inputs from code simulations, these studies inferred the decay rate of the target electrostatic potential. In our experiments the availability of multiple particle types with different velocities, in addition to multiple shots with different fusion burn histories, allows the time evolution of the target potential to be mapped out with minimal *a priori* assumptions about conditions in the plasma.

While particles may gain energy in the low-density corona, they can lose energy during passage through the high-density target plasma. The fundamental physics of particle energy loss in a plasma is of vital importance to ICF. In particular, for ignition in an ICF capsule, theoretical predictions indicate that areal densities (ρR) exceeding 300 mg/cm^2 are required to stop 3.5 MeV alphas in DT fuel at ~ 10 keV.[9] Also, a number of charged-particle ρR diagnostics rely on stopping power calculations in order to interpret the measured particle energy shifts.[10–12] Although there is general agreement among different theoretical formulations for stopping powers in plasmas,[13–15] there have only been a few attempts to verify these predictions.[16–19] In addition, previous measurements were compromised by the uncertainties of either partially ionized plasmas[16,17] (in which the charge state of the background plasma was not known precisely) or unknown charge states of the incident particle[18,19] (usually a heavy ion). In the experimental stopping power tests described in this paper, both these uncertainties are

[a]Present address: Lawrence Livermore National Laboratory, Livermore, CA 94550; electronic address: hicks13@llnl.gov
[b]Visiting Senior Scientist at the Laboratory for Laser Energetics, University of Rochester.

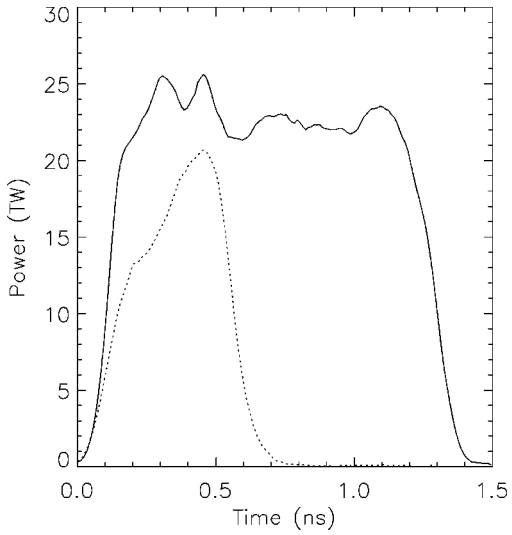

FIG. 1. Characteristic shapes for laser pulses. The dotted line shows the 0.4 ns pulse with 8 kJ total energy; the solid line shows the 1.0 ns pulse with 27 kJ of total energy.

eliminated by using light ions in conditions typical of exploding pusher targets where the shell and fuel are essentially fully ionized. Using simultaneous measurements of four different fusion products which have velocities above and below thermal electron velocities, these measurements provide the first experimental verification of the general form of stopping power predictions over a wide velocity range.

In these studies, two types of laser conditions were used to irradiate thin, glass-shell targets. The first used a 1.0 ns, high-energy (27 kJ) pulse in which the fusion burn occurred during the pulse. In this case the energy shifts were dominated by electrostatic acceleration. Most of the analysis in this paper will be devoted to discussing how the measured energy shifts for the various particles can be interpreted in terms of a time-decaying potential. The second used a 0.4 ns, low-energy (8 kJ) laser pulse where the fusion products were produced when the electric fields had essentially decayed away. The measured downshifts of the fusion products were then dominated by slowing down in the target.

II. EXPERIMENTS

The experiments were performed on the OMEGA laser system at the Laboratory for Laser Energetics, University of Rochester. OMEGA is a 60-beam, neodymium-doped phosphate glass laser capable of delivering 30 kJ of frequency-tripled, 0.35 μm light.[1] Irradiation uniformity is accomplished using distributed phase plates and 2D (two dimension) smoothing by spectral dispersion with a bandwidth of 0.2 THz.[20] Including the effects of beam-to-beam energy variations, the estimated illumination uniformity for 60 overlapping beams was $\sim 5\% - 10\%$. Two types of laser pulse were used in these studies: A 0.4 ns full-width at half maximum (FWHM) pulse with a total energy of ~ 8 kJ, and a 1 ns flat top pulse with a total energy of ~ 27 kJ. The average, on-target laser intensity was 7×10^{14} W/cm^2 and 1×10^{15} W/cm^2 for the short and long pulses, respectively. Examples of these two pulse shapes are shown in Fig. 1.

Targets were 900–950 μm diameter glass microballoons with wall thicknesses ranging from 2.3 to 3.0 μm. They were filled with a mixture of 5 atm D_2 and 10 atm of ^{3}He (where fill pressures are given at 300 K) to give a 1:1 atomic ratio of D:^{3}He fuel.

The protons and tritons from the D+D reaction as well as the protons and alphas from the D+^{3}He reaction were used in this study. These reactions and the nominal energy of their products are shown below:

$$\mathrm{D+D} \rightarrow T(1.01\ \mathrm{MeV}) + p(3.02\ \mathrm{MeV}), \tag{1}$$

$$\mathrm{D+{}^3He} \rightarrow \alpha(3.67\ \mathrm{MeV}) + p(14.68\ \mathrm{MeV}). \tag{2}$$

Spectra were observed using a charged-particle spectrometer[21] consisting of a 7.6 kG permanent magnet with CR-39 nuclear track-etch detectors. The instrument has an energy range of 0.1–40 MeV and can measure fusion product yields between 10^7 and 10^{14}. Yields up to 10^{16} can be measured for fast ions at energies <1 MeV. A variable collimator size assists in achieving this high dynamic range. Different particle species with the same gyroradius produce different size tracks and can thus be easily discriminated. For example, protons at 3 MeV, tritons at 1 MeV, and alphas at 3 MeV all have the same gyroradius but the alphas record the largest tracks, and the protons the smallest.[22] With the high-fusion yields attained in these experiments (10^{10} to 10^{11}), the energy measurement uncertainties were dominated by systematic rather than statistical errors. The energy calibration was established by using the measured magnetic fields in a particle tracking code whose predictions have been verified at the 3 and 14.7 MeV proton position using differential ranging filters. A rapid, automated scanning system was developed which can readily count 10^6 tracks per shot, although typically only 10^3 to 10^4 are required for accurate spectra.

Simultaneous measurements can be made by two similar spectrometers positioned 101° apart, one outside the OMEGA chamber at 235 cm from the target (CPS-1), the other inside at 100 cm (CPS-2). For many purposes, these two instruments allow measurement symmetries to be assessed. For these studies, where highly accurate, simultaneous measurements of four spectral lines were required, there was a reasonable probability that part of the spectrum could land in the dead space between detectors, potentially compromising the energy measurement.[23] For this reason, the presence of two spectrometers (each with a very slightly different field configuration and thus energy calibration) usually allowed at least one instrument to record all four lines successfully.

In addition to CPS-1 and CPS-2, some neutron diagnostics were utilized. DD neutron yields were measured using indium activation, ion temperatures were derived from neutron time-of-flight measurements of the 2.45 MeV DD neutrons and some peak neutron bang times were measured using the neutron temporal diagnostic (NTD).[24]

III. MEASUREMENTS

Spectra from a 0.4 ns and a 1 ns pulse shot are shown in Figs. 2 and 3. The measured quantities (yield, mean energy,

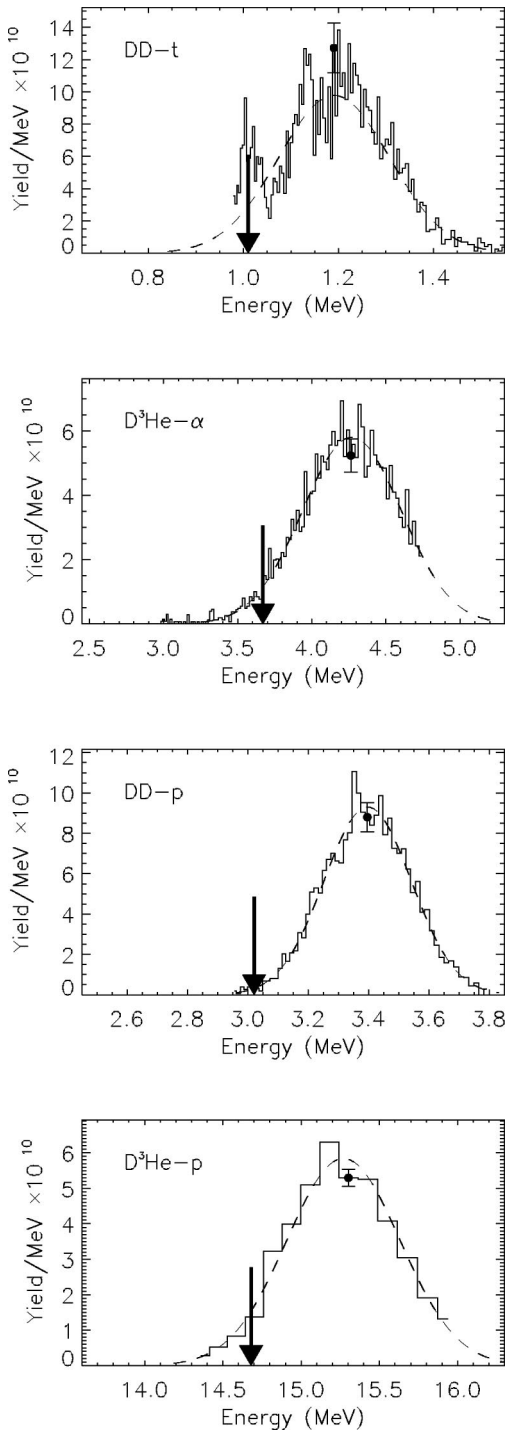

FIG. 2. DD and D^3He particle spectra measured by CPS-2 from a shot with a 1.0 ns pulse width (shot 13 804) clearly showing the energy upshifts. Arrows indicate the nominal birth energy. A sample error bar is shown on each spectrum that gives the statistical uncertainty in one channel.

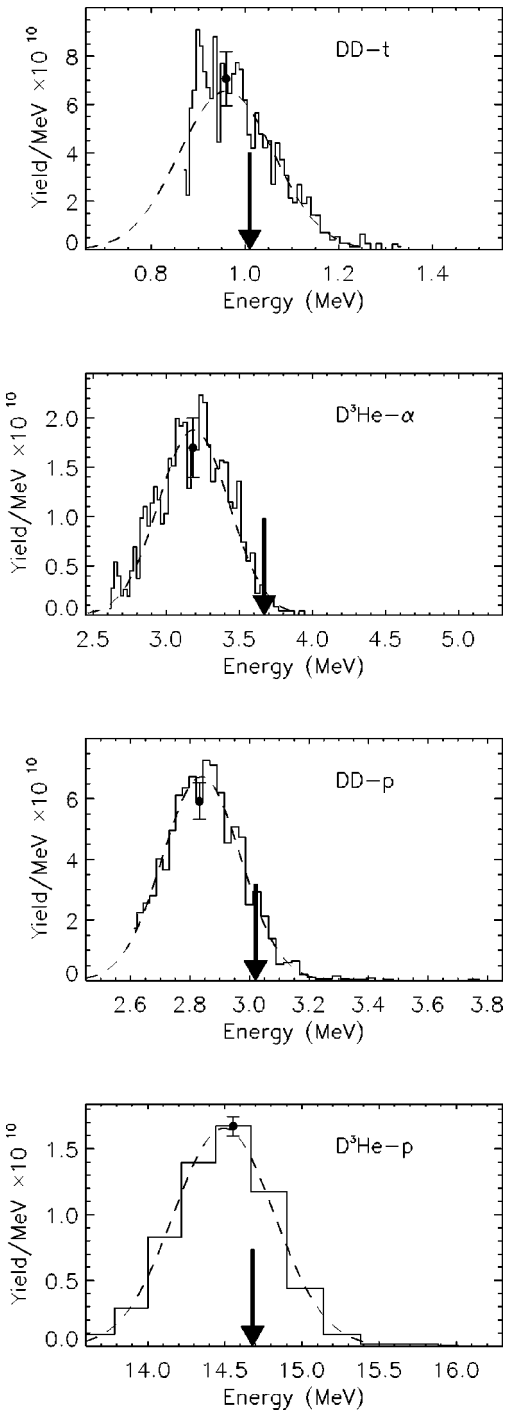

FIG. 3. DD and D^3He particle spectra measured by CPS-1 from a shot with a 0.4 ns pulse width (shot 16 176) clearly showing the energy downshifts. Arrows indicate the nominal birth energy. A sample error bar is shown on each spectrum that gives the statistical uncertainty in one channel.

line width) are determined from values given by the best-fit Gaussian. A summary of the shot parameters and measurements are shown in Table I.

As mentioned earlier, the number of particles counted in each spectrum ($>10^3$) was large enough that statistical errors in mean-energy measurements were small in comparison to systematic uncertainties in the energy calibration. Best estimates indicate that systematic errors are ~60 keV for 3 MeV protons and 3.7 MeV alphas, ~20 keV for 1 MeV tritons, and ~100 keV for 14.7 MeV protons. On a number of shots not shown here, the peak region of one or more of the four spectra was lost in the detector dead space and the mean energy could not be determined with sufficient accuracy. Results shown in Table I are only those for which all four spectral lines could be observed on one instrument or the other. The spectra shown in Figs. 2 and 3 also contain

TABLE I. Summary of results for shots where the four relevant DD and D^3He particles were measured. The yield, mean energy (E), and standard deviation (σ) of the spectral lines were determined using a best-fit Gaussian. Available maximum fast proton energies are noted for completeness.

Shot no.	13786	13804	13825	16176
Laser energy (kJ)	28.4	27.7	26.8	8.4
Pulse width (ns)	1.0	1.0	1.0	0.4
Target diameter (μm)	903.6	903.4	921.0	925.0
Shell thickness (μm)	2.3	2.7	3.0	2.5
Bang time[a] (ns)	0.81	0.92	1.00	0.82
Ion temp. (keV)	12.0	13.2	11.6	9.4
DD neutron yield	2.96E10	4.18E10	5.15E10	2.04E10
CPS	1	2	2	1
Yield (DD-*t*)	2.99E10	2.86E10	5.52E10	1.66E10
Yield (DD-*p*)	3.73E10	3.39E10	3.50E10	2.24E10
Yield (D^3He-α)	5.30E10	4.87E10	3.93E10	1.14E10
Yield (D^3He-*p*)	3.49E10	5.28E10	4.92E10	1.35E10
E(DD-*t*) (MeV)	1.47	1.19	1.04	0.96
E(DD-*p*)	3.54	3.40	3.29	2.84
E(D^3He-α)	4.69	4.27	3.88	3.19
E(D^3He-*p*)	15.2	15.3	15.1	14.6
σ(DD-*t*) (MeV)	0.161	0.116	0.129	0.101
σ(DD-*p*)	0.154	0.145	0.135	0.133
σ(D^3He-α)	0.287	0.336	0.330	0.245
σ(D^3He-*p*)	0.26	0.31	0.29	0.27
Fast E_{max} (MeV)	n/a	0.85	0.76	0.43

[a]Bang times for the 1 ns shots were calculated; for the 0.4 ns shot it was measured. When both calculated and measured bang times are available, they are generally in good agreement.

minor gaps; however, the losses were small enough that they did not compromise the measurements.

Individual lines measured accurately on both spectrometers showed that the difference in mean energy measurements between the two instruments was generally accounted for by experimental errors. This indicated that no detectable asymmetry in the mean particle energies was present on the thin-shell glass targets used in these studies.

The yield measurements indicate that fusion products from the same reaction (DD tritons and protons, or D^3He alphas and protons) have measured yields that can differ from each other by as much as 50%, even though typical statistical uncertainties are $<3\%$. These nonstatistical fluctuations, which are believed to be due to asymmetric particle fluxes, are typical of charged-particle yield measurements on OMEGA and have been noted in previous work.[22] Since the studies described here do not require absolute yield values, these asymmetries will not affect the results.

The line widths quoted in Table I have the instrument broadening, caused by the finite collimator width, removed. This effect is negligible for all but the D^3He proton line where the instrument broadening is $\sim 20\%$. Although most line shapes were closely approximated by a Gaussian, the DD triton spectra of Fig. 2 had noticeable non-Gaussian features. These features, which generally appear only in DD triton spectra, are not understood at present, though they could be associated with the fast proton spectra with energies up to ~ 0.8 MeV that are observed on these shots. The tritons (unlike the other higher-velocity fusion products) have velocities comparable to these protons. Limited fast proton spectra were recorded on these specific shots but a general description of fast proton measurements on OMEGA is given elsewhere.[25]

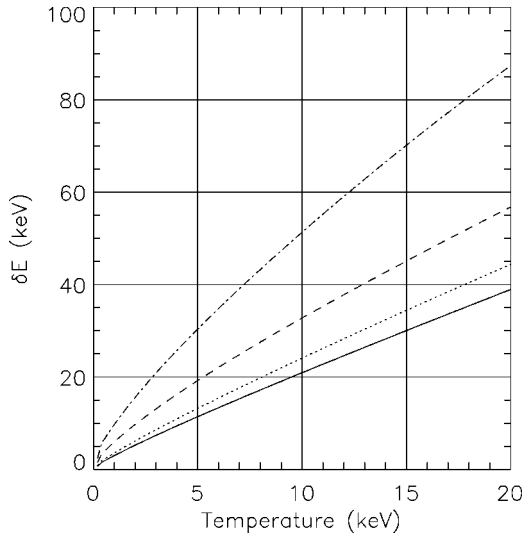

FIG. 4. Finite temperature corrections to the energies of fusion products as found using the formulation of Brysk (Ref. 27). The particle types shown are: DD tritons (solid), D^3He alphas (dotted), DD protons (dashed), and D^3He protons (dot–dashed). Although small compared to the total particle energy, at fuel ion temperatures of ~ 10 keV these corrections are of the same order as instrument uncertainties and need to be added to the nominal energies shown in Eqs. (1) and (2).

On many shots similar to those listed in Table I, bang times recorded using the NTD were in excellent agreement with those from the 1D (one-dimensional) hydrodynamics code LILAC.[26] For the particular 1.0 ns shots where good charged-particle spectra were obtained, the NTD was unavailable and no data were recorded. The bang times listed in Table I for the 1.0 ns shots were, therefore, determined from simulations, while that for the 0.4 ns shot was measured by the NTD. Bang times are given with respect to the start of the laser pulse, on the time scale given in Fig. 1. In the following analysis, these are the only results utilized that were derived from simulations.

IV. ANALYSIS

Before proceeding with the study of energy shifts, it is necessary to consider the effect of finite temperature corrections to particle birth energies. For fuel ion temperatures of order 10 keV, corrections to the zero temperature values shown in Eqs. (1) and (2) are of the same order as instrumental errors and thus need to be included. Figure 4 shows these corrections for the particle types and reactions as determined using the formulation of Brysk.[27]

With these corrections, the calculated energy shifts, ΔE are shown in Fig. 5. Results show that using the 1.0 ns pulse, $\Delta E \geqslant 0$ whereas using the 0.4 ns pulse, $\Delta E < 0$. This clearly indicates that with the longer pulses acceleration is dominant while with the shorter pulse energy losses are dominant.

A. Electrostatic acceleration

The electrostatic acceleration of ions in laser-produced plasmas is generally caused by hot electrons escaping from the surface of the irradiated material and producing strong

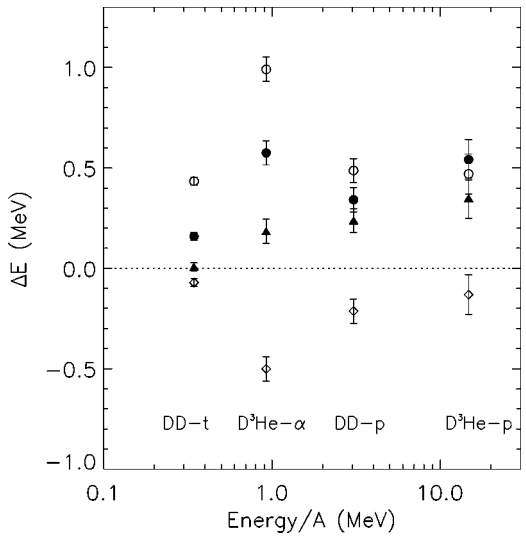

FIG. 5. Energy shifts for the four particle types measured on the four different shots shown in Table I. Shots with 1.0 ns pulse widths are shown with open circles (shot 13 786), filled circles (shot 13 804) and solid triangles (shot 13 825). Shot 16 176, with the 0.4 ns pulse width, is shown with diamonds. Throughout this paper, these same plot symbols will be used to identify the same shots. Note that, on all 1.0 ns shots, the shifts were positive, whereas on the 0.4 ns shot, shifts were negative.

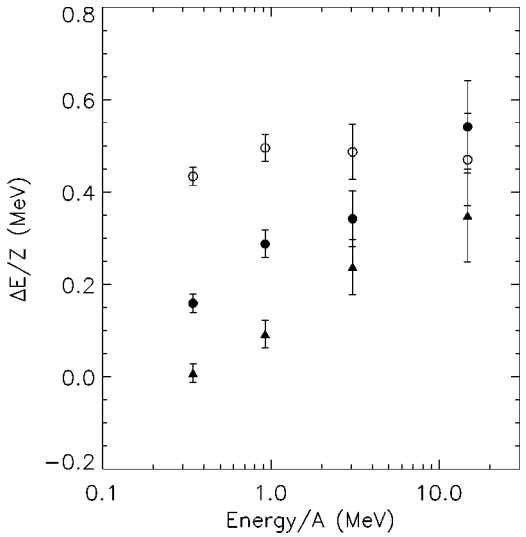

FIG. 6. The measured energy upshifts for the four different particle types on the three shots with 1 ns pulses. The upshifts (normalized to Z) increase for higher velocity particles and are greater for shots with earlier bang times. Shots with bang times at 0.81, 0.92, and 1.00 ns are represented by the open circles, filled circles, and triangles, respectively. These symbols correspond to the same shots as in Fig. 5.

electric fields.[3,4] In a spherical implosion, creation of these fields in the corona cause the inside of the capsule to acquire a positive potential with respect to the outside. Fusion products produced near the target center thus gain energy when they emerge from the capsule. In these experiments, the observed upshifts indicate that the targets have potentials up to about 0.5 MV when the fusion burn occurs. This high potential is unexpected given the laser intensities of $\sim 10^{15}$ W/cm^2 and wavelength of 0.35 μm used on OMEGA and the origin of such a high potential is still unclear.[25] The following discussion is intended to use the energy shifts of different particles to measure the time history of the electrostatic potential. In the future, this result may provide some clues as to why such high potentials exist in the first place.

To study the electrostatic acceleration of fusion products, we consider data from the 1.0 ns pulse shots and plot $\Delta E/Z$ versus E/A in Fig. 6, where ΔE is the net energy shift, E is the birth energy, Z is the charge number, and A is the mass number of each of the particle types. Two trends are apparent. Firstly, for a given particle type, smaller upshifts are generally found on shots with later bang times. Such behavior was observed before using DT alphas and attributed to an electrostatic potential decaying with time.[8] Secondly, on any given shot, slower particles have upshifts that are generally less than (or at most similar to) those for faster particles. The following analysis will show that this behavior can also be interpreted in terms of a time-decaying electrostatic potential as long as the electric field region is located far enough from target center to introduce the necessary time-of-flight differences among particles of different velocities. Slower particles reach the decaying fields at later times than the faster ones and experience less acceleration. Using a simple model to describe the field region, these data allow the time history of the electrostatic potential to be determined.

In this analysis, the electrostatic potential and its variation with time is assumed to be the same for all three shots. Justification for this comes from examining the laser and target parameters for the three 1.0 ns pulse shots. The data in Table I show that the rms (root-mean-square) laser energy difference among the shots is 2.9% which is small compared to the shell thickness and bang time rms differences of 13.2% and 10.4%, respectively. Assuming that it is the laser conditions which are primarily responsible for determining the time history of the potential, similar laser conditions mean that different energy shifts can be attributed to particles sampling the potential at different times (and, to a much lesser extent, variations in energy losses in the target), rather than the potential changing from shot to shot.

In order to interpret the data a simple model will be utilized to allow the energy shift, ΔE, to be related to the initial particle velocity, v, and bang time, t_b. With suitable approximations, these experimentally measured values can be related through the electrostatic potential, $\phi(t)$, and some free model parameters. An optimization procedure will be used to determine these free parameters, and hence $\phi(t)$, taking into account energy losses due to slowing down in the target.

The model used in this analysis assumes that the electric fields are restricted to a region of finite width, δ, located some distance, $D(t)$, away from target center and moving with fixed velocity, v_D. Physically this describes how the fields are confined to the corona region outside the target and are expanding with a velocity characteristic of the fast ions. The subsequent analysis will show that the inferred velocity is more likely to be that of the heavier fast ions rather than the fast protons. The potential distribution, $\phi(r,t)$, of this model is shown schematically in Fig. 7. For $0 \leqslant r \leqslant D(t)$

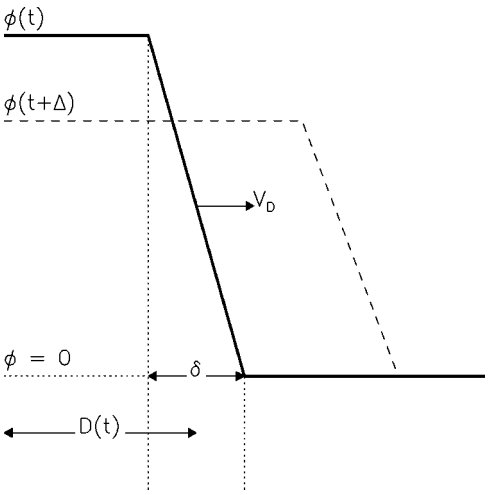

FIG. 7. Schematic of model for electrostatic potential as a function of position. The potential at target center is $\phi(t)$ and decays as a function of time. The field region is centered at a position $D(t)$ away from target center, has a width δ, and moves with a velocity v_D.

$-\delta/2$, where r is the distance from target center, $\phi(r,t)=\phi(t)$ and is constant in space (though decaying in time); for $r \geqslant D(t)+\delta/2$ the potential is zero. The change in potential, which occurs over the width δ centered at $r=D(t)$, is, for simplicity, taken to decrease linearly with r. In the discussion below, we will refer to this field region as a ''sheath,'' although this is not required to be the same as a Debye sheath.

It can be shown (see Appendix A) that particle energy shifts are generally insensitive to the value of δ. In light of this, it is convenient to set δ to zero to simplify the analysis. This allows the energy shifts to be expressed simply in terms of the electrostatic potential:

$$\frac{\Delta E^i}{eZ^i}=\frac{v^i}{v^i-v_D}\phi(t_D^i), \tag{3}$$

where the superscript i refers to a particular spectral line measurement and t_D^i is the time when particles of type i reach the sheath center, $D(t)$. If the sheath position is given by $D(t)=D_0+v_D(t-t_0)$, where t_0 is an arbitrary time taken to be 1 ns in this analysis, and the particle position is given by $r^i=v^i(t-t_b^i)$, then $t_D^i=(D_0+v^i t_b^i-v_D t_0)/(v^i-v_D)$.

Equation (3) thus allows $\phi(t)$ to be determined at various times t_D^i as long as the free parameters D_0 and v_D are specified. To illustrate how these free parameters can be estimated using the data at hand, Fig. 8 shows $\phi(t)$ for a few values of D_0 when $v_D=0$. It is apparent that only when $D_0 \simeq 1$ mm do the data from all shots align to give a continuously decaying potential. This optimal D_0 will change for other values of v_D. More generally, by varying both parameters, the optimal value of D_0 and v_D can be determined.

This optimization procedure requires a figure-of-merit to be defined which quantifies the degree of ''alignment'' of the data. One such quantity is the goodness-of-fit parameter, χ^2, calculated for the best fit of a function to the data. Without *a priori* knowledge of the form of $\phi(t)$, it is reasonable to approximate this function by the first few terms in a Taylor expansion. In this analysis $\phi(t)$ will be approximated by a second-order polynomial. The calculated χ^2 for a range of D_0 values with $v_D=0$ is plotted in Fig. 9 and shows that χ^2 has a well-defined, global minimum close to $D_0=1$ mm.

To complete this optimization procedure, the effects of particle slowing down in the target need to be considered, although energy losses in these thin-glass targets are expected to be small compared to the measured upshifts. With some assumptions, the unknown energy losses can be reduced to one additional free parameter which may be optimized along with D_0 and v_D. In the general case, unknown energy losses in the three different targets with different shell thicknesses would introduce six new unknowns—areal density (ρR) and temperature (T) for all three targets. To simplify this, all shots are assumed to have a temperature of 2.8 keV (based on the inferred temperature found in the next section). ρR's for the 2.3, 2.7, and 3.0 μm thick shells are assumed to be 0, $\rho R_{\max}/2$, and $\rho R_{\max}$, respectively. Final results are not sensitively dependent upon the value of T, the ratios of the different ρR's, or on whether $\rho R=0$ for the thinnest-shell target. These crude assumptions are reasonable because the energy losses in these targets represent only a small correction to the total inferred upshifts. Using these values of ρR and T, energy losses can be estimated with the stopping formula shown in the next section [Eq. (4)].

With these simplifications, the optimization procedure becomes one of finding the global minimum in χ^2 by varying 3 parameters: D_0, v_D, and $\rho R_{\max}$. Calculating χ^2 for a range of input parameters shows that a well-defined, global minimum exists at $D_0=2.1$ mm, $v_D=3.7$ mm/ns, and $\rho R_{\max}=2.3$ mg/cm^2. Contour plots showing the variations of χ^2 in three slices through this minimum are shown in Fig. 10. Each successive contour moving outwards from the minimum corresponds to $\Delta\chi^2=+1$. At its minimum, the reduced χ^2 is 1.0—as required for a successful fit.

It is interesting to examine the physical significance of the inferred sheath velocity. This velocity of 3.7 mm/ns, corresponds to an energy of $\sim$70 keV/nucleon. This is considerably below the speed of the highest energy fast protons ($\sim$800 keV/nucleon) and makes it likely that this velocity is related to that of the heavier fast ions (such as Si and O). Future studies might investigate whether different shell materials affect this inferred velocity. Interestingly, previous numerical studies have shown that the strongest electric fields in an expanding plasma exist in a very narrow sheath centered on the leading edge of an expanding fast ion species.[28,29] The inferred velocity of $v_D=3.7\times10^8$cm/s would then be the velocity of the fastest heavy ions whose leading edge is located at $D_0=2.1$ mm at $t_0=1.0$ ns. The maximum energy of the heavy ions could be determined in the future using this spectrometer which has made some preliminary measurements of such particles.

The inferred electrostatic potential, determined by the solution at $\chi^2_{\min}$, is given by $\phi(t)=1.6-1.6t+0.4t^2$, where $\phi(t)$ is in MV and t in ns. The result is shown in Fig. 11. As

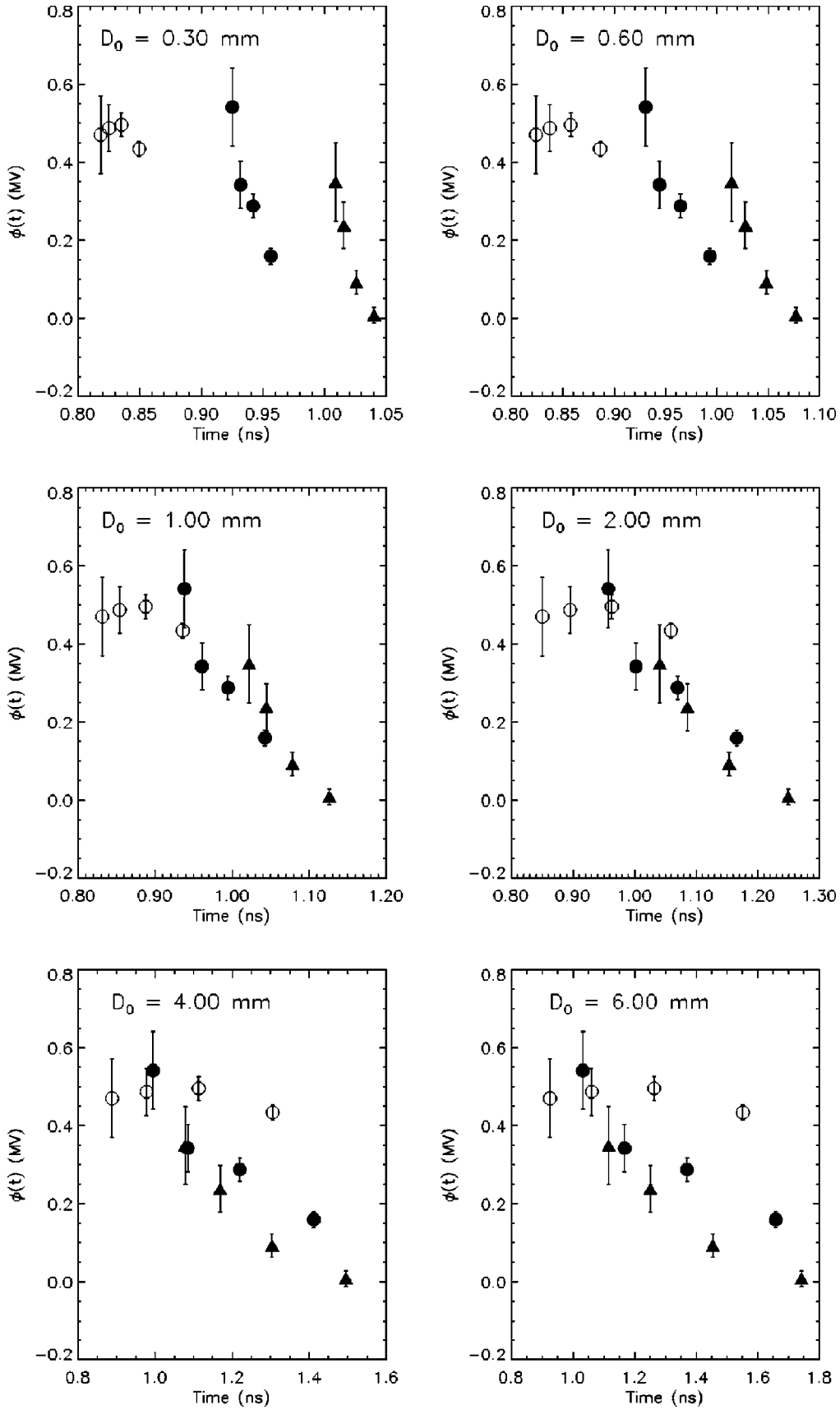

FIG. 8. The inferred $\phi(t)$ if the sheath center is fixed at a variety of distances, D_0, from target center. In these figures both the sheath velocity, v_D, and energy losses in the target are set to zero. Note how the data align themselves when $D_0 \simeq 1$ mm. Plot symbols are as in Fig. 6. With $v_D = 0$, the data points from shot 13 786 (open circles) give a potential roughly constant in time; however, with a nonzero v_D, as in Fig. 11, these points give a decaying potential.

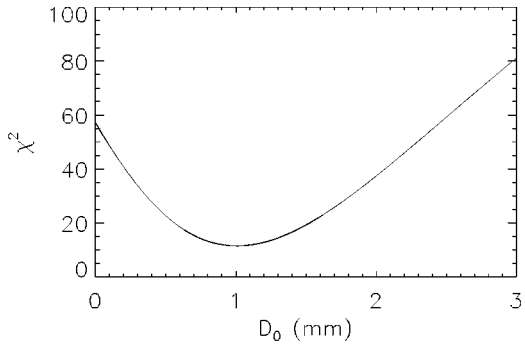

FIG. 9. The variation of the goodness-of-fit parameter, χ^2, with D_0 for a quadratic fit to $\phi(t)$ assuming $v_D=0$ and no energy losses in the target. As might be expected from Fig. 8, χ^2 has a minimum close to $D_0=1$ mm. At this minimum, the reduced χ^2 is 1.9.

described earlier, the analytic form of this potential should be regarded as the first three terms in a Taylor expansion of $\phi(t)$. For this reason, the result should not be expected to be valid outside the time interval covered by the data.

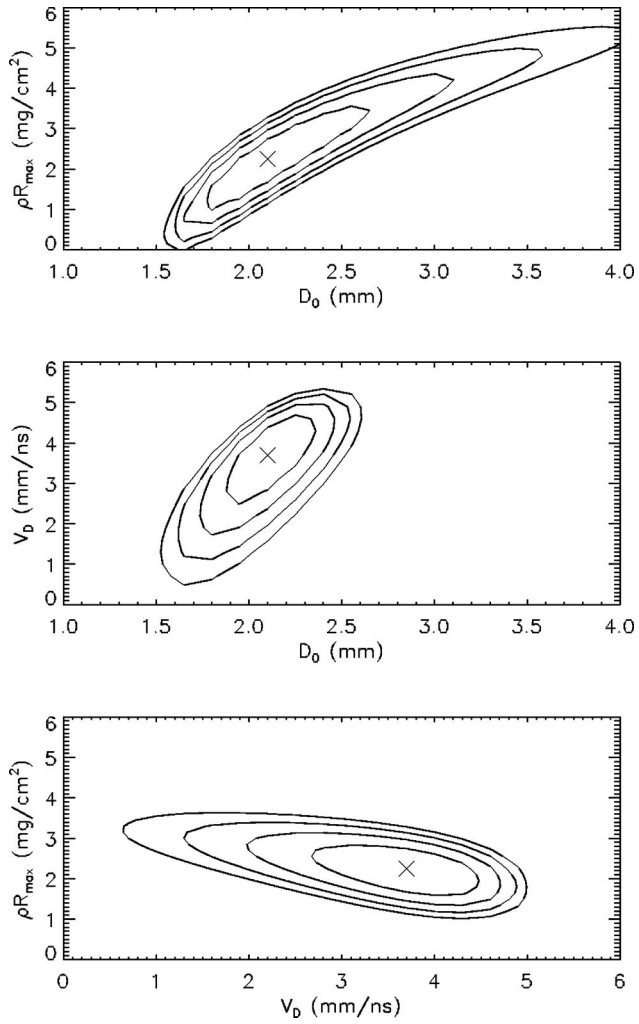

FIG. 10. Contour plots of χ^2 showing the variation with the three parameters, D_0, V_D, and $\rho R_{\max}$. All three contour slices intersect at the global minimum of $\chi^2=6.2$ indicated by the crosses. Each successive contour moving outwards from the minimum χ^2 corresponds to an increment in χ^2 of $+1$.

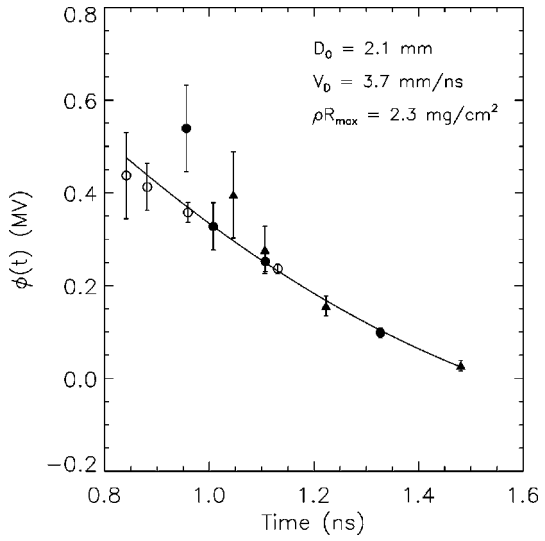

FIG. 11. The potential, $\phi(t)$, which gives the best fit to all the data is $\phi(t)=1.6-1.6t+0.4t^2$. This corresponds to $D_0=2.1$ mm, $v_D=3.7$ mm/ns, and $\rho R_{\max}=2.3$ mg/cm^2.

It can be seen from Fig. 11 that the potential has dropped to <0.1 MV at 1.4 ns, which corresponds to the end of the laser pulse (see Fig. 1). This is important for the study of fusion product energy shifts on thick-shell implosions, where the bang time occurs at >1.5 ns.[12] For such experiments, it appears valid to assume that all measured energy shifts can be attributed to losses in the target.

The decay of the potential could be the result of a number of factors, including the expansion of fast ions and subsequent decrease of electric fields, cessation of hot electron production, the cooling of hot electrons due to expansion, or the presence of neutralizing currents from the stalk that holds the target. In the above analysis, only a generic model of the accelerating field region has been used, without any *a priori* assumptions about the hot electron temperature, density gradient, or other plasma parameters. Further analysis will be able to determine how this measured potential can be related to such plasma parameters, and may be able to ascertain which of the mechanisms described above play significant roles in discharging the target potential.

B. Stopping power of charged particles in plasmas

In this section, charged-particle stopping powers will be examined using energy shifts measured on the shorter pulse, 0.4 ns shot. From Fig. 5 it is clear that the spectral downshifts observed on this shot are in marked contrast to the upshifts observed when the longer, 1 ns pulses were used. Assuming that spectral shifts due to acceleration are negligible compared to those due to energy losses, it will be shown that the measured shifts can be understood based purely on the effects of charged-particle slowing down in the target. This confirms that the assumption of negligible acceleration is indeed a reasonable one.

The slowing down of charged particles in a plasma is strongly dependent upon the velocity of the incident, or test, particles. Depending on the relative magnitude of the test

particle velocity, v_t, and the thermal velocity of the background electrons, $v_{\rm th}$, the plasma can be described as ''cold'' ($v_t \gg v_{\rm th}$), ''warm'' ($v_t \sim v_{\rm th}$), or ''hot'' ($v_t \ll v_{\rm th}$). Theoretical predictions of charged-particle stopping powers show general agreement for cold plasmas but small differences for warm and hot plasmas.[13–15] These theories all predict the same fundamental velocity dependence: stopping powers should reach a maximum when $v_t \simeq v_{\rm th}$. Experimental tests of these theories have been confined mostly to cold plasmas.[16,17] A few studies have been done in warm plasmas though these measurements were compromised by uncertainties in the charge state of the incident heavy ions.[18] In the experiments described in this paper, the four different fusion products have velocities which are both greater and less than typical electron thermal velocities (corresponding to temperatures of a few keV), allowing the three plasma regimes, from hot to cold, to be probed on a single shot. These measurements confirm for the first time the presence of the peak in stopping power when test particle and thermal electron velocities are similar.

The general form for the charged-particle energy loss per unit distance, dE/dx, in fully ionized plasmas may be given by[13–15]

$$-\frac{1}{Z^2}\frac{dE}{dx}=\left(\frac{\omega_p e}{v_t}\right)^2\left[G\left(\frac{v_t^2}{v_{\rm th}^2}\right)\ln\Lambda+H\left(\frac{v_t}{v_{\rm th}}\right)\right], \tag{4}$$

where $\omega_p=(4\pi n_e e^2/m_e)^{1/2}$ is the electron plasma frequency, Z is the projectile charge number, v_t is the velocity of the incident particle, $v_{\rm th}=(2T/m_e)^{1/2}$is the thermal velocity of the plasma electrons, and $\ln\Lambda$ is the Coulomb logarithm;[30] n_e, e, and m_e are the electron density, charge, and mass respectively. For compatibility with previous treatments, Gaussian units have been used. $G(x)=\mathrm{erf}(x^{1/2})-2(x/\pi)^{1/2}e^{-x}$ is the Chandrasekhar function (where the large-angle scattering terms are small and can be neglected[31]). This function peaks at $x\simeq 1$, and explains why the stopping power reaches a maximum when $v_t \simeq v_{\rm th}$. The small differences that arise among various stopping models come from the form of $H(v_t/v_{\rm th})$ and generally only occur where $v_t < v_{\rm th}$. The formulation given above is for stopping by plasma electrons; a similar formulation gives the stopping by plasma ions, which, for conditions of interest here, is $<10\%$ of stopping by electrons.

From Eq. (4) it can be seen that for particles of different charge number, Z, and mass number, A, ranging through the same plasma conditions, the energy loss normalized to Z^2 is a function almost exclusively of the particle velocity, v_t. Any explicit dependence on A is small and confined to the slowly varying Coulomb logarithm. Consequently, a useful way to compare the energy loss of particles with different energies, charge, and mass that pass through the same material is to plot $-\Delta E/Z^2$ versus E/A (proportional to v_t^2), where E is the particle birth energy. In this fashion, the data from the 0.4 ns shot are shown in Fig. 12.

To test how well these measured shifts are described by stopping power theories, Eq. (4) is integrated over an assumed areal density, ρR, and fit to the data using ρR and T as free parameters. The best fit is found for $\rho R=4.5$ mg/cm^2 and $=2.8$ keV (errors in these values will be discussed below). The result is shown in Fig. 12 and illustrates how the data do indeed confirm the general form of the stopping power curves spanning the velocity range from $v_t \ll v_{\rm th}$ to $v_t \gg v_{\rm th}$. The resulting peak in stopping power when $v_t \simeq v_{\rm th}$ is evident in the data.

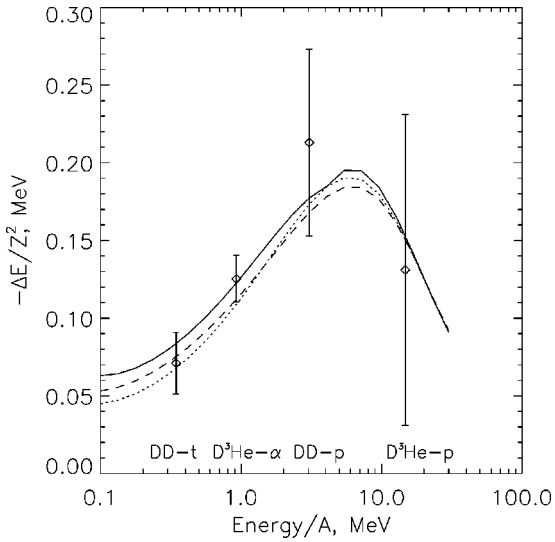

FIG. 12. Measured energy losses for the 0.4 ns shot 16 176. The best fit of the Li and Petrasso (Ref. 15) stopping theory to these data is shown as a solid line and was found to give $\rho R=4.5$ mg/cm^2 and $T=2.8$ keV. Using these values of ρR and T, the predictions of two other models are shown for reference: Mehlhorn (Ref. 13) (dotted line), and Peter and Meyer-ter-Vehn (Ref. 14) (dashed line). In these curves, the slowing down is assumed to occur in a fully ionized plasma. Although electron stopping is dominant, ion stopping is also included.

A few important assumptions were required in order to calculate the curves in Fig. 12. Firstly, the calculations assumed that energy losses occurred in a fully ionized plasma. For $T>1$ keV, Saha equilibrium predicts that the average charge of an SiO_2 plasma is $\bar{Z}>9.5$ indicating that the plasma is, to good approximation, fully ionized. Secondly, the ion number density was assumed to be 10^{22} /cm^3. Its precise value is not critical since for a given value of ρR it influences the stopping power only through the slowly varying Coulomb logarithm. Thirdly, the inferred ρR and T are determined assuming that all energy losses occur in the glass shell. Only small corrections to the inferred total ρR arise if some losses also occur in the fuel.

Having shown that fusion product energy shifts in this type of experiment are well-described by stopping power theories, it is worthwhile examining how accurately such energy shift measurements determine the value of ρR and T. To do this, the goodness-of-fit parameter, χ^2, found by fitting Eq. (4) to the data in Fig. 12, is computed for a range of ρR and T values. The results are displayed as a contour plot in Fig. 13 with the position of the minimum χ^2, used for the fit in Fig. 12, shown by the cross. Each successive contour moving outwards from this minimum corresponds to $\Delta\chi^2=+1$. The limits within which ρR and T can be found to a 68% confidence level are given by the extremes of the in-

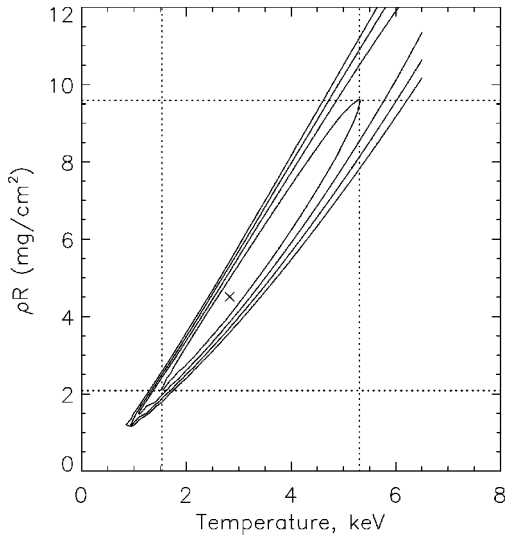

FIG. 13. Contours of χ^2 in ρR and T space found by fitting the data in Fig. 12 to stopping power predictions. The minimum value of the reduced χ^2 is 0.9 and is found at $\rho R = 4.5$ mg/cm^2 and $T = 2.8$ keV (shown by the cross). Each successive contour moving out from this minimum represents an increment of $\Delta\chi^2 = +1$. The dotted lines represent the limits within which ρR and T are determined to a 68% confidence level.

nermost contour (corresponding to $\chi^2 = \chi^2_{\min} + 1$) and illustrated by the dotted lines. The inferred areal density and temperature, with accompanying errors, are thus given by $\rho R = 4.5^{+5.1}_{-2.4}$ mg/cm^2 and $T = 2.8^{+2.5}_{-1.3}$ keV.

The uncertainties in ρR and T would be reduced by decreasing the error in the 14.7 MeV D ^{3}He proton line shift measurement. The high velocity of this particle means that its energy loss is very insensitive to T and is determined almost exclusively by ρR. An accurate measure of its energy shift thus directly provides a ρR measurement. The line shifts of the other particles would then allow a more precise estimate of T. In general, the percentage errors in each of the line shift measurements could be decreased through use of a thicker shell target (for which all particles still emerge). Such a target would cause greater downshifts in the spectra. Since the systematic errors are independent of the total downshift, the percentage errors would be reduced.

Another way to reduce uncertainties in the inferred areal density and temperature is through the use of additional fusion products. The 9.5 MeV deuteron produced in the T+ ^{3}He reaction and the 0.8 MeV ^{3}He particle produced in the D+D reaction would provide additional data points in the warm and hot plasma regimes, respectively. Both these particle types have already been observed using this spectrometer.

Incorporating these improvements may provide sufficient constraints on the stopping power curves to differentiate among the different stopping models.

V. CONCLUSIONS AND FURTHER WORK

The use of multiple charged fusion products to probe the conditions in laser-produced plasmas has been shown to be extremely valuable. These particles are test probes which essentially do not perturb the surrounding plasma. Simultaneous measurements of fusion products with four different velocities produced in spherical implosions has allowed the time history of the target electrostatic potential to be determined and the validity of fundamental charged-particle stopping theories to be tested. Using a 27 kJ, 1 ns flat top pulse to irradiate a thin-glass-shell microballoon, the fusion products were generated near the end of the pulse and had energy upshifts of up to ~ 0.5 MeV per unit charge. A simple model of the electric field region was used to infer the evolution of the target potential with minimal *a priori* assumptions about the plasma conditions and no inputs from simulations. This potential was found to disappear soon after the laser was turned off. Using a 0.4 ns, 8 kJ laser pulse on a similar target, where the fusion products were generated after completion of the pulse, particle energy losses were dominated by the effects of slowing down in the target. Comparing the energy shifts of these particles has provided the first experimental verification of the velocity dependence of charged-particle stopping theories. The velocities of the four fusion products were both greater and less than typical electron thermal velocities, allowing the expected peak in the stopping power to be observed. Verification of stopping power theory justifies the use of energy loss measurements for diagnosing areal density.[11,12]

In the future, analysis of the acceleration process needs to account for the production of fast protons. Unlike the fusion products, fast ions probably cannot be treated as test particles since they almost certainly modify the electric fields. With energies higher than the upshifts of the fusion products it is likely that these particles are produced early in the pulse when electric fields are greatest. Unifying the phenomena of fast ion and fusion particle acceleration may allow the entire time history of the target potential to be found, starting at the beginning of the pulse. This might provide some clues as to why a potential of order one megavolt exists on these targets in the first place, and what mechanisms lead to its discharge.

The asymmetries in yield measurements of the different fusion products were mentioned only briefly in this paper. The source of these asymmetries is still unclear but it is reasonable to suspect that they arise from electric or magnetic fields in the corona. To test this hypothesis, a study might examine whether the amplitude of these yield fluctuations decreases on targets with later bang times.

Improvements in the energy loss measurements would be achieved by using shots with thicker shells which produce greater spectral downshifts, and hence smaller percentage errors in the shift measurements. In addition, the use of the 9.5 MeV deuteron from T+^{3}He reactions and the 0.8 MeV ^{3}He particle from D+D reactions, both of which have already been measured, would place further constraints on the shape of the stopping power curves. This would enable ρR and T to be determined with greater accuracy. Importantly, such added constraints may be able to test which of the different stopping models is valid.

ACKNOWLEDGMENTS

This work was supported in part by LLE sub contract number PO410025G, LLNL sub-contract number B313975,

the U.S. Department of Energy Contract Number DE-FG03-99SF21782, and the U.S. Department of Energy Office of Inertial Confinement Fusion under Cooperative Agreement No. DE-FC03-92SF19460.

APPENDIX A: DETERMINING THE ELECTROSTATIC POTENTIAL

The energy shift, ΔE, of a particle passing through the sheath shown in Fig. 7 is given by integrating the Lorentz equation

$$\frac{\Delta E}{eZ} = \int_{t_1}^{t_2} \epsilon_0(t) v \, dt, \tag{A1}$$

where $\epsilon_0(t)$ is the electric field inside the sheath, v is the initial velocity of the particle, and t_1 and t_2 are the times at which the particle enters and exits the sheath respectively. In this model, the electric field is assumed to be constant throughout the sheath, but varying in time. If the change in velocity of the particle is small compared to the initial velocity, as is the case for all measurements in this experiment, the nonlinearities in Eq. (A1) can be removed to give:

$$\frac{\Delta E}{eZ} = v \int_{t_1}^{t_2} \epsilon_0(t) dt, \tag{A2}$$

where v is the initial velocity of the particle. With this approximation, t_2 can be found simply by using the initial velocity of the particle to compute directly the transit time through the sheath.

For a sheath moving at a constant velocity, $D(t) = D_0 + v_D(t - t_0)$, where D_0 is the position at an arbitrary time t_0, which will be taken to be 1 ns. Since the position of a particle, $r(t)$, generated at a time t_b and traveling with velocity v is given by $r(t) = v(t - t_b)$, the time, t_D, at which the particle reaches the center of the sheath is given by

$$t_D^i = \frac{D_0 + v^i t_b^i - v_D t_0}{v^i - v_D}, \tag{A3}$$

where the superscript i refers to particles with a specific velocity v and bang time t_b, or, in other words, a given spectral line from a particular shot. It is then found that $t_1^i = t_D^i - t_\delta^i/2$ and $t_2^i = t_D^i + t_\delta^i/2$, where $t_\delta^i = \delta/(v^i - v_D)$ is the time to traverse the sheath. Describing the electric field variation with time as a polynomial, $\epsilon_0(t) = \Sigma_{n=0}^N a_n t^n$, substituting this in Eq. (A2), and using the expressions for t_1 and t_2 gives

$$\frac{\Delta E^i}{eZ^i} = v^i \sum_{n=0}^{N} \frac{a_n}{n+1} \left[\left(t_D^i + \frac{t_\delta^i}{2} \right)^{n+1} - \left(t_D^i - \frac{t_\delta^i}{2} \right)^{n+1} \right]. \tag{A4}$$

Although this provides a general expression relating the energy shift to particle velocities and bang times, it is more convenient to express ΔE in terms of the target electrostatic potential. Since $\epsilon_0(t)$ is assumed to be constant throughout the sheath, the potential at the center of the target is given simply by $\phi(t) = \epsilon_0(t)\delta$, or

$$\phi(t) = \sum_{n=0}^{N} b_n t^n, \tag{A5}$$

where $b_n = a_n \delta$ and N is the order of the polynomial. Multiplying out Eq. (A4) and using Eq. (A5) gives

$$\frac{\Delta E^i}{eZ^i} = \frac{v^i}{v^i - v_D} \left[\sum_{n=0}^{1} \phi_n(t_D^i) + \sum_{n=2}^{N} \phi_n(t_D^i)(1 + \mathcal{P}_n(\epsilon^i)) \right], \tag{A6}$$

where $\phi_n(t_D) = b_n t_D^n$, $\epsilon = t_\delta / t_D$, and

$$\mathcal{P}_n(\epsilon) = \sum_{k=3}^{n+1} \frac{1}{n+1} \binom{n+1}{k} \epsilon^{k-1} \left(\frac{1 - (-1)^k}{2^k} \right).$$

This is the general expression relating the energy shift to the target potential. It can thus be seen that if $\epsilon \ll 1$ then $\mathcal{P}_n(\epsilon) \ll 1$ and Eq. (A6) can be simplified to

$$\frac{\Delta E^i}{eZ^i} = \frac{v^i}{v^i - v_D} \phi(t_D^i). \tag{A7}$$

Importantly, if $\phi(t)$ is linear [$\phi_n = 0$ for $n \geq 2$ in Eq. (A6)] then Eq. (A7) is exact regardless of the value of ϵ. This means that, even though the acceleration may occur over some finite sheath width, the results are mathematically equivalent to treating the acceleration as occurring over an infinitesimal sheath. In the studies reported in this paper, the inferred $\phi(t)$ is given by $\phi(t) = 1.6 - 1.6t + 0.4t^2$, indicating that the function is in fact close to linear over the time interval covered by the data. This means that the assumption that $\delta = 0$ used in the analysis in Sec. IV A is valid. Note that this also means the data cannot be used to infer anything about the value of δ.

APPENDIX B: LINE BROADENING EFFECTS

The analysis in Sec. IV A focused on interpreting shifts of the spectral lines in terms of a decaying potential. The presence of a decaying electrostatic potential might also be expected to cause a broadening of the spectral lines. In particular, the finite burn period means that similar particles produced at different times would acquire different energy shifts. Also, the kinematic broadening of the nascent energy spectrum means that even particles produced at the same time may have sufficient time-of-flight separation when they reach the accelerating sheath to gain different energy shifts. Both of these effects would make the line widths wider than could be accounted for by Doppler broadening alone. In this section, this extra broadening will be shown to be small.

In Fig. 14, the variance of the spectral width, $\Delta\sigma^2$, that remains after subtraction of the DD-neutron-determined Doppler contribution (the data in Table I already have instrument broadening removed) are indeed generally greater than zero. $\Delta\sigma^2$ is determined by subtracting the variance of the Doppler width from that of the measured width. Generally, the line width measurements are better for the DD protons and D ^{3}He alphas since the DD triton lines are perturbed by anomalous structure, and the lower dispersion makes precision measurement of the D ^{3}He proton lines more difficult. Measurement errors are $\sim 5\%$ for the charged-particle spectral widths and the neutron spectral widths.

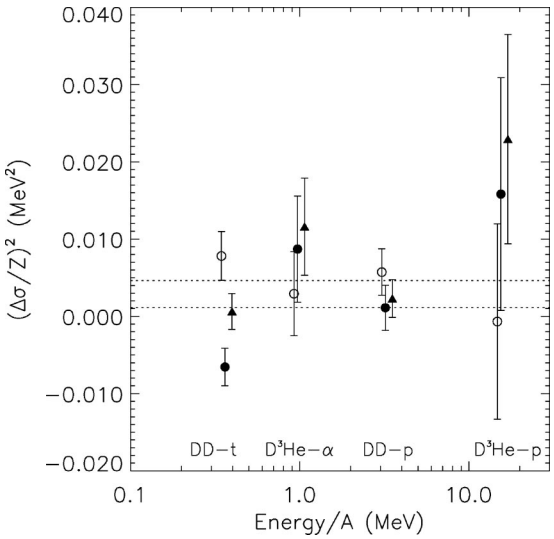

FIG. 14. The variance of the spectral line width, $\Delta\sigma^2$, that remains after subtracting contributions from Doppler broadening. Data points with the same Energy/*A* are separated artificially to allow their individual error bars to be distinguished. The dotted lines show the predicted broadening if the particles are produced over a FWHM burn period between 0.1 and 0.2 ns and the potential decays at an average rate of -0.8 MV/ns as predicted in Fig. 11.

To predict how much a decaying potential would broaden spectra, consider that typical burn periods for these shots are $\tau=0.1$ to 0.2 ns at FWHM. This would cause an extra broadening of $\Delta\sigma/Z=(\tau/2.35)|\mathrm{d}\phi/\mathrm{d}t|$. Additional broadening due to the time-of-flight dispersion of Doppler-shifted particles traveling $D\sim 2$ mm is generally much smaller and may be neglected. Assuming an average decay rate of $|\mathrm{d}\phi/\mathrm{d}t|=0.8$ MV/ns determined from Fig. 11 gives the predicted range of $(\Delta\sigma/Z)^2$ shown in Fig. 14 by the dotted lines. This expected broadening is roughly consistent with measurements, especially those for the DD protons, though substantial scatter exists in the data.

[1]T. R. Boehly, D. L. Brown, R. S. Craxton *et al.*, Opt. Commun. **133**, 495 (1997).
[2]J. M. Soures, R. L. McCrory, C. P. Verdon *et al.*, Phys. Plasmas **3**, 2108 (1996).
[3]J. E. Crow, P. L. Auer, and J. E. Allen, J. Plasma Phys. **14**, 65 (1975).
[4]Y. Kishimoto, K. Mima, T. Watanabe, and K. Nishikawa, Phys. Fluids **26**, 2308 (1983).
[5]T. H. Tan, G. H. McCall, and A. H. Williams, Phys. Fluids **27**, 296 (1984).
[6]S. J. Gitomer, R. D. Jones, F. Begay, A. W. Ehler, J. F. Kephart, and R. Kristal, Phys. Fluids **29**, 2679 (1986).
[7]Y. Gazit, J. Delettrez, T. C. Bristow, A. Entenberg, and J. Soures, Phys. Rev. Lett. **43**, 1943 (1979).
[8]J. Delettrez, A. Entenberg, Y. Gazit, D. Shvarts, J. Virmont, T. Bristow, J. M. Soures, and A. Bennish, Nucl. Fusion **23**, 1135 (1983).
[9]J. D. Lindl, *Inertial Confinement Fusion* (Springer-Verlag, New York, 1998).
[10]Y. Kitagawa, K. A. Tanaka, M. Nakai *et al.*, Phys. Rev. Lett. **75**, 3130 (1995).
[11]R. D. Petrasso, C. K. Li, M. D. Cable *et al.*, Phys. Rev. Lett. **77**, 2718 (1996).
[12]C. K. Li, D. G. Hicks, F. H. Séguin *et al.*, Phys. Plasmas **7**, 2578 (2000).
[13]T. A. Mehlhorn, J. Appl. Phys. **52**, 6522 (1981).
[14]T. Peter and J. Meyer-ter-Vehn, Phys. Rev. A **43**, 1998 (1991).
[15]C. K. Li and R. D. Petrasso, Phys. Rev. Lett. **70**, 3059 (1993).
[16]F. C. Young, D. Mosher, S. J. Stephanakis, S. A. Goldstein, and T. A. Mehlhorn, Phys. Rev. Lett. **49**, 549 (1982).
[17]J. N. Olsen, T. A. Mehlhorn, J. Maenchen, and D. J. Johnson, J. Appl. Phys. **58**, 2958 (1985).
[18]J. Jacoby, D. H. H. Hoffmann, W. Laux *et al.*, Phys. Rev. Lett. **74**, 1550 (1995).
[19]M. Roth, C. Stöckl, W. Sü*β*, O. Iwase, D. O. Gericke, R. Bock, D. H. H. Hoffmann, M. Geissel, and W. Seelig, Europhys. Lett. **50**, 28 (2000).
[20]S. Skupsky and R. S. Craxton, Phys. Plasmas **6**, 2157 (1999).
[21]D. G. Hicks, C. K. Li, R. D. Petrasso, F. H. Séguin, B. E. Burke, J. P. Knauer, S. Cremer, R. L. Kremens, M. D. Cable, and T. W. Phillips, Rev. Sci. Instrum. **68**, 589 (1997).
[22]D. G. Hicks, Ph.D. Thesis, Massachusetts Institute of Technology (1999).
[23]The CR-39 is divided into multiple, flat pieces arranged in a curve in the dispersion region to ensure nearly normal particle incidence over the entire energy range. Slight gaps between adjacent pieces mean that ~15% of the area behind the magnet is dead space.
[24]R. A. Lerche, D. W. Phillion, and G. L. Tietbohl, Rev. Sci. Instrum. **66**, 933 (1995).
[25]D. G. Hicks, C. K. Li, F. H. Séguin *et al.*, ''Observations of fast protons above 1 MeV produced in laser-fusion experiments,'' Physics of Plasmas (to be published).
[26]M. C. Richardson, P. W. McKenty, F. J. Marshall *et al.*, in *Laser Interaction and Related Plasma Phenomena*, edited by H. Hora and G. H. Miley (Plenum, New York, 1986), Vol. 7, p. 421.
[27]H. Brysk, Plasma Phys. **15**, 611 (1973).
[28]J. Denavit, Phys. Fluids **22**, 1384 (1979).
[29]Ch. Sack and H. Schamel, Plasma Phys. Controlled Fusion **27**, 717 (1985).
[30]J. D. Huba, *NRL Plasma Formulary* (U.S. Naval Research Laboratory, Washington, DC 1998).
[31]C. K. Li and R. D. Petrasso, Phys. Plasmas **2**, 2460 (1995).